

# The 1/3 Geometric Constant: Scale Invariance and the Origin of 'Missing Energy' in 3D Quantum Fragmentation

Jinzen Zhu\*

Physics Department, Ludwig Maximilians Universität, D-80333 Munich, Germany and  
Shanghai Artificial Intelligence Laboratory, 129 Longwen Road, Shanghai, China

We report a fundamental geometric constraint on the detection of kinetic energy release (KER) in three-dimensional quantum fragmentation. By investigating the sudden dissociation of Slater-type orbitals—a physically motivated basis for localized states—we demonstrate that the ratio of the peak detected energy to the integrated mean,  $R_E = E_{\text{peak}}/\langle E \rangle$ , is strictly bounded below 0.5 for all physical parameter spaces. We systematically map the behavior of  $R_E$  across the orbital localization ( $\zeta$ ) and effective repulsive charge ( $Q$ ) landscape. Our results show that while  $R_E$  exhibits sensitivity to the force-field geometry at atomic scales, it converges to a remarkably stable, scale-invariant constant of  $\approx 0.33$  in the high-localization limit ( $M \propto \zeta$ ) characteristic of subatomic ground states ( $n = 1, Q = 1$ ). This 1/3 geometric constant provides a provocative first-principles interpretation of the historical “missing energy” problem in nuclear physics. We suggest that the 1/3 average energy ratio observed in Beta decay spectra may be a topological artifact of the  $4\pi r^2$  volume weighting inherent to 3D wavefunctions, rather than exclusively a signature of undetected mass. This work establishes  $R_E < 0.5$  as a universal geometric baseline for quantum simulations and offers a new framework for reconstructing the true energy budget in subatomic calorimetry by correcting for the intrinsic masking effects of 3D radial geometry.

PACS numbers: 32.80.-t, 32.80.Rm, 32.80.Fb

## I. INTRODUCTION

The sudden approximation remains a cornerstone of quantum dynamics, providing a robust framework for systems where an instantaneous change in the Hamiltonian occurs before the wavefunction can spatially redistribute [1, 2]. This regime is particularly critical in the study of Coulomb explosions and nuclear dissociations, where rapid transitions from attractive to repulsive potentials lead to the fragmentation of the system. Historically, classical and 1D semiclassical models have been the primary tools for interpreting the resulting kinetic energy release (KER) [3]. However, these models frequently struggle to replicate the precise energy distributions observed in high-resolution experiments, often overestimating the detected peak energy and failing to account for significant portions of the integrated energy budget.

In this work, we demonstrate that the persistent discrepancy between theoretical energy conservation and experimental observation is a fundamental consequence of 3D quantum geometry. By utilizing a local energy framework applied to Slater-type orbitals (STOs)—the physical standard for localized quantum systems—we show that the energy distribution  $P(E)$  is governed by the  $4\pi r^2$  radial volume weighting. A primary finding of this study is the “0.5 Rule”: the ratio of the peak detected energy to the integrated statistical mean ( $R_E = E_{\text{peak}}/\langle E \rangle$ ) is strictly bounded below 0.5 for ground-state configurations. This shift occurs because the 3D volume element

suppresses the probability density near the potential energy singularity at the origin, a geometric effect that 1D simulations inherently fail to capture.

To establish the universality of this phenomenon, we perform an exhaustive parametric study across the principal quantum number ( $n$ ), the orbital exponent ( $\zeta$ ), and the repulsive charge ( $Q$ ). Crucially, we investigate the scaling limit where the particle mass  $M$  is proportional to the localization parameter  $\zeta$ . Under these conditions, we uncover a scale-invariant regime where the ratio  $R_E$  converges to a stable constant, which is  $\approx 0.33$  for a repulsive unit charge ( $Q = 1$ ).

This 1/3 geometric constant provides a provocative re-interpretation of the “missing energy” problem in subatomic physics. Just as the beta-decay crisis of the early 20th century necessitated the neutrino to satisfy energy conservation based on an observed 1/3 average energy ratio [4, 5], our results suggest that such imbalances may be an intrinsic signature of the initial state’s 3D geometry. If the detected peak inherently captures only one-third of the true interaction energy due to radial sequestering, then “missing” energy may represent the recovered high-momentum components of the primary fragment rather than undetected mass. This work establishes a necessary geometric baseline for interpreting energy calorimetry across atomic, nuclear, and high-energy scales.

\* zhujinzenlmu@gmail.com

## II. THEORETICAL METHODOLOGY

### A. The Sudden Approximation and Potential Inversion

The core of our model rests on the sudden approximation, which is valid when a system's Hamiltonian changes on a timescale  $\tau_{perturb}$  much shorter than the characteristic response time of the quantum state:

$$\tau_{perturb} \ll \frac{\hbar}{\Delta E} \quad (1)$$

where  $\Delta E$  represents the energy spacing of the system. Under this condition, the initial wavefunction  $\psi_0(\mathbf{r})$  remains "frozen" at  $t = 0$ , as there is insufficient time for the probability density to reorganize [1, 2].

In the context of a Coulomb explosion, the potential undergoes an instantaneous transition from an attractive configuration to a repulsive one:

$$V_{initial}(r) = -\frac{Z_{att}}{r} \longrightarrow V_{final}(r) = +\frac{Q}{r} \quad (2)$$

This approximation effectively captures the dynamics of ultrafast processes such as multi-photon ionization by attosecond pulses, core-hole creation followed by Auger decay, or the sudden loss of strong-force confinement in nuclear physics.

### B. Bohmian Local Energy Formulation

To determine the kinetic energy distribution of the resulting fragments, we utilize the de Broglie-Bohm formulation of quantum mechanics. In this framework, the total energy  $E(\mathbf{r})$  of a particle at a specific spatial coordinate  $\mathbf{r}$  is defined by the sum of the repulsive potential and the local kinetic energy density  $T_{local}(\mathbf{r})$ :

$$E(\mathbf{r}) = T_{local}(\mathbf{r}) + V_{final}(\mathbf{r}) \quad (3)$$

The local kinetic energy is derived from the Laplacian of the initial spatial wavefunction:

$$T_{local}(\mathbf{r}) = -\frac{\hbar^2}{2m} \frac{\nabla^2 \psi_0(\mathbf{r})}{\psi_0(\mathbf{r})} \quad (4)$$

For the Slater-type orbitals (STOs) investigated in this work, defined by the radial form  $R(r) = N r^{n-1} e^{-\zeta r}$ , the Laplacian in spherical coordinates yields the following analytical expression for the local kinetic energy:

$$T_{local}(r) = \frac{\hbar^2}{2m} \left( \zeta^2 - \frac{2n\zeta}{r} + \frac{n(n-1)}{r^2} \right) \quad (5)$$

Combining this with the repulsive potential, we obtain the conserved total energy for a trajectory starting at radius  $r$ :

$$E(r) = \frac{\hbar^2}{2m} \left( \zeta^2 - \frac{2n\zeta}{r} + \frac{n(n-1)}{r^2} \right) + \frac{Q}{r}. \quad (6)$$

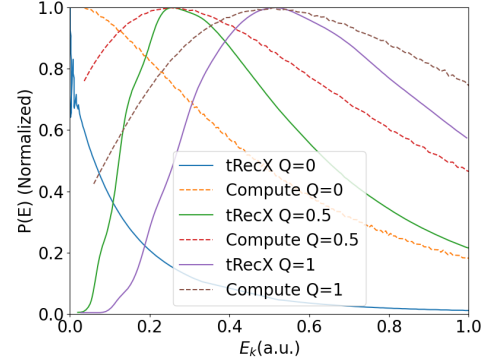


FIG. 1. Comparison of normalized energy distributions  $P(E)$  between the present model (solid) and tRecX TDSE simulations (dashed). Results are shown for repulsion charges  $Q = 0, 0.5$ , and using an initial 1s hydrogenic orbital ( $\zeta = 1, l = 0$ ). Peak positions show high consistency across all charge values.

### C. Numerical Implementation and Statistical Weighting

The final observable energy distribution  $P(E)$  is constructed by sampling the initial positions according to the 3D radial probability density:

$$\rho(r) = 4\pi r^2 |\psi_0(r)|^2 \quad (7)$$

By mapping each sampled coordinate  $r$  to its corresponding energy  $E(r)$ , we generate a histogram weighted by  $\rho(r)$ . Because each Bohmian particle conserves its total energy along its trajectory in a time-independent repulsive field, the energy distribution calculated at the instant of the potential flip ( $t = 0$ ) is identical to the asymptotic kinetic energy distribution measured by detectors at  $t \rightarrow \infty$ .

This methodology avoids the computational complexity of solving the Time-Dependent Schrödinger Equation (TDSE) while preserving the critical 3D geometric information—namely the  $r^2$  volume weighting—that is lost in simplified 1D models.

## III. DISTRIBUTION PROPERTY

To validate the predictive power of our 3D Bohmian-based model, we compared the resulting energy distributions  $P(E)$  against full quantum simulations performed via the tRecX [6–11] software package. We utilized a standard 1s Slater orbital ( $\zeta = 1, l = 0$ ) as the initial state and varied the repulsive Coulomb charge  $Q$ .

As shown in Figure 1, the peak positions calculated by our method are in excellent agreement with the tRecX benchmarks across all charge values ( $Q \in \{0, 0.5, 1\}$ ), the shape of our distribution is also similar to tRecX computation. The deviations in the distribution tails

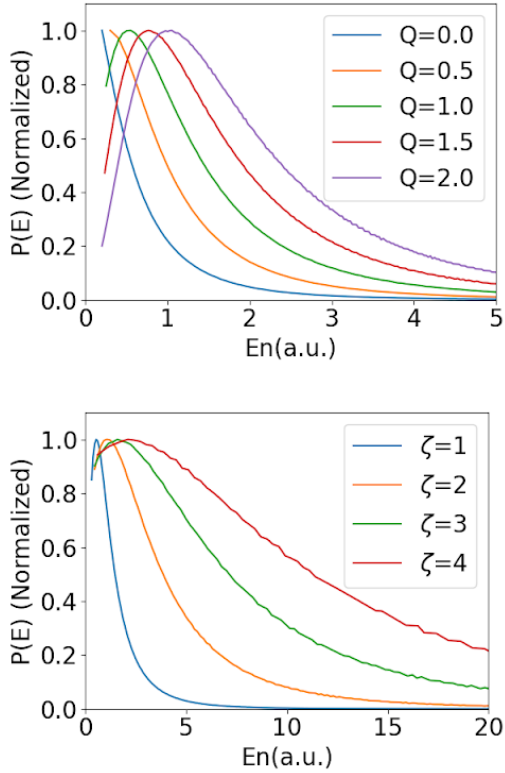


FIG. 2. Parametric evolution of the energy distribution  $P(E)$ . (Upper) Variation with repulsive Coulomb charge  $Q \in [0, 2]$  for a fixed 1s orbital ( $\zeta = 1, l = 0$ ). Both the peak position and spectral width increase with  $Q$ . (Lower) Variation with orbital exponent  $\zeta \in [1, 4]$  at a fixed charge  $Q = 1$ . The distribution broadens more rapidly with increasing  $\zeta$  compared to  $Q$ , highlighting the sensitivity of the KER to initial state localization.

are attributed to the numerical constraints of grid-based solvers. Specifically, the truncation of the Coulomb potential and the use of polynomial quadrature grids in tRecX often struggle to resolve the singularity at  $r \rightarrow 0$ , whereas our analytical local-energy approach maintains precision in the near-nucleus region. This consistency in peak prediction confirms that our simplified method effectively captures the primary experimental signatures of the Coulomb explosion.

To characterize the influence of the system's physical parameters on the detected energy, we performed a systematic study varying the repulsive Coulomb charge  $Q$  and the orbital exponent  $\zeta$ .

As illustrated in Figure 2 (Upper), increasing the repulsive charge  $Q$  leads to a systematic shift in the energy distribution  $P(E)$  toward higher energies. This is accompanied by a significant broadening of the spectral width. Since the local energy is defined as  $E(r) = T_{local}(r) + Q/r$ , a larger  $Q$  increases the potential gradient across the spatial extent of the orbital, thereby spreading the resulting energy values over a wider range.

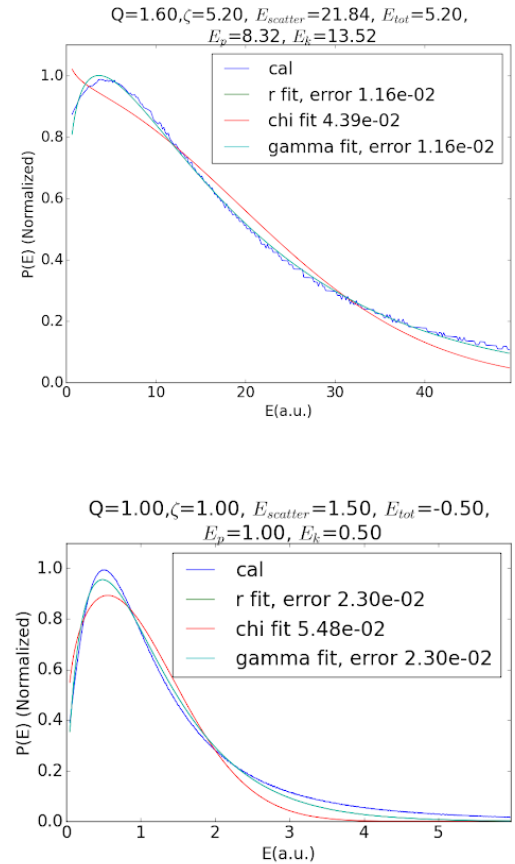


FIG. 3. Analytical fitting and energy comparison of  $P(E)$ . (Upper) Results for  $\zeta = 1, Q = 1, l = 0$ ; (Lower) Results for  $\zeta = 5.2, Q = 1.6, l = 0$ . The r-fit (green) and Gamma fit (cyan) show the lowest error (<2%), identifying the radial nature of the distribution.  $E_p$  and  $E_k$  denote integrated potential and kinetic energies, while Escatter represents the total energy in the repulsive regime. In all cases,  $E_{peak}$  remains substantially lower than Escatter.

In Figure 2 (Lower), we examine the effect of the orbital exponent  $\zeta$  while maintaining a constant charge ( $Q = 1$ ). We observe that the peak position of  $P(E)$  is highly sensitive to the spatial localization of the initial state. As  $\zeta$  increases, the wavefunction becomes more tightly bound, which simultaneously increases the local kinetic energy density  $T_{local} \propto \zeta^2$  and places the particle density in regions of higher potential energy. Interestingly, the distribution broadens much more rapidly with respect to  $\zeta$  than it does with respect to  $Q$ . This suggests that the internal "quantum pressure" (local kinetic energy) of the initial state plays a more dominant role in determining the final energy dispersion than the external repulsive force itself.

To identify a universal analytical form for the fragment energy spectrum, we performed a regression analysis on the energy distribution  $P(E)$  using several statisti-

cal models. Figure 3 illustrates the results for a ground-state hydrogenic orbital ( $\zeta = 1, Q = 1$ ) and a more localized, higher-charge configuration ( $\zeta = 5.2, Q = 1.6$ ).

We compared the computed data (blue) against three candidate distributions: a radial-type distribution (r-fit), a Gamma distribution, and a distribution. As shown in the figure, the r-fit (green) and the Gamma distribution (cyan) produce the highest fidelity, with a residual error of less than 2%. The near-perfect overlap between these two functions confirms that the energy distribution essentially obeys a radial distribution law.

A critical quantitative observation is found in the integrated energy values shown in the plot headers. In both cases, the peak energy  $E_{peak}$  is significantly smaller than the total scattering energy Escatter (the integrated average  $\langle E \rangle$ ). Specifically, for the  $\zeta = 1, Q = 1$  case, the “energy conservation” value  $\langle E \rangle$  is driven higher by the potential energy density near the origin, whereas the experimental peak corresponds to the most probable radial position. This discrepancy validates our hypothesis that fragment detectors fundamentally probe the radial geometry of the initial state rather than the integrated energy mean.

#### IV. SCALING LAWS AND THE ENERGY DETECTION DISCREPANCY

To quantify the discrepancy between experimentally observed fragment signals and theoretical energy conservation, we define the energy detection ratio as:

$$R_E = \frac{E_{peak}}{\langle E \rangle} \quad (8)$$

where  $E_{peak}$  is the mode of the distribution  $P(E)$  and  $\langle E \rangle$  is the integrated average (expectation value) of the total energy. This dimensionless ratio serves as a metric for the “skewness” of the distribution and the efficiency with which a detector captures the system’s total energy.

Figure 4 illustrates the systematic evolution of  $R_E$  across a broad parametric space of repulsive charges ( $Q$ ) and orbital exponents ( $\zeta$ ).

##### A. Influence of Repulsive Charge $Q$

As shown in the upper panel of Figure 4,  $R_E$  increases monotonically with the repulsive charge  $Q$ , asymptotically approaching a limit of 0.5. In the high- $Q$  regime, the repulsive potential  $V = Q/r$  dominates the local kinetic energy terms. This “classicalization” of the potential landscape shifts the peak of the distribution closer to the statistical mean. However, the fact that  $R_E$  remains strictly bounded below 0.5 underscores that the 3D quantum spatial spread of the Slater orbital is an inescapable constraint on the fragment energy spectrum.

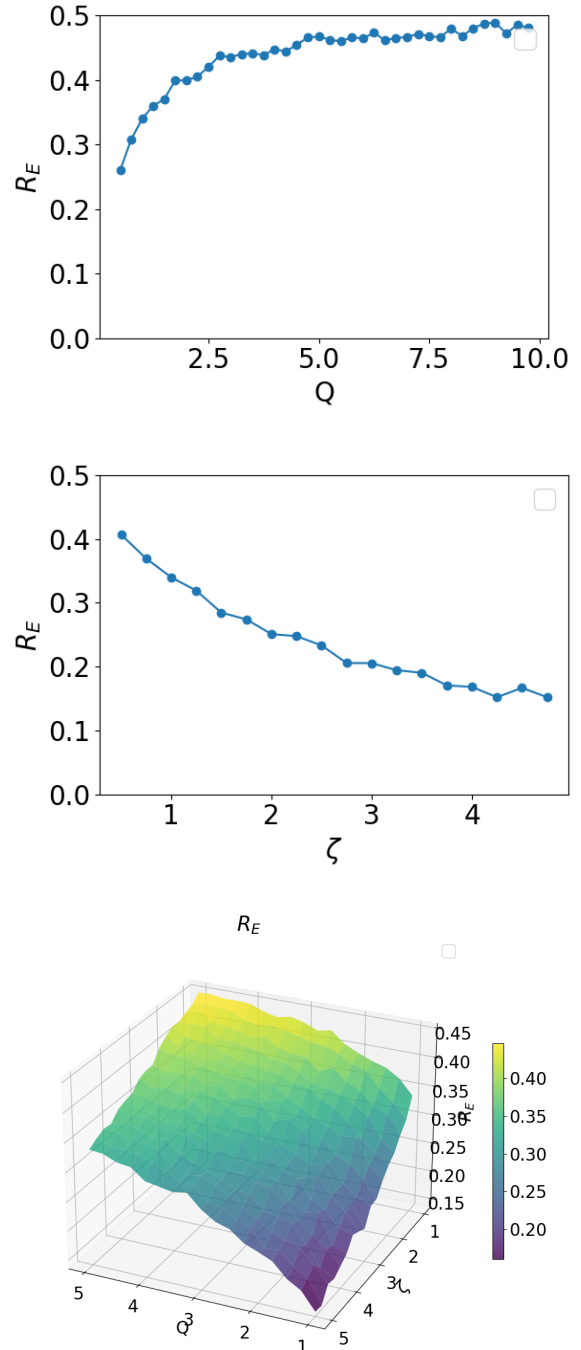


FIG. 4. Universal scaling of the peak-to-mean energy ratio  $R_E = E_{peak}/\langle E \rangle$ . (Upper) Variance with repulsive charge  $Q$  at  $\zeta = 1$ , showing monotonic convergence toward 0.5 as the repulsive potential dominates. (Middle) Variance with orbital exponent  $\zeta$  at  $Q=1$ , showing a precipitous drop in detection efficiency for localized states. (Lower) Contour map of  $R_E(\zeta, Q)$ . The ratio is strictly bounded below 0.5, with the greatest discrepancy occurring for inner-shell analogs (high  $\zeta$ ). High  $\zeta$  values correspond to deeper initial potentials where the “quantum pressure” ( $T_{local}\zeta^2$ ) significantly skews the average energy relative to the experimental peak.

## B. Orbital Exponent $\zeta$ : Inner-Shell vs. Outer-Shell Dynamics

The middle panel of Figure 4 demonstrates a precipitous decline in  $R_E$  as the orbital exponent  $\zeta$  increases. In the framework of Slater-type orbitals,  $\zeta$  serves as a proxy for the effective nuclear charge and the principal quantum number ( $\zeta \approx Z_{\text{eff}}/n$ ). Consequently, small  $\zeta$  values represent diffuse outer-shell (valence) orbitals, while large  $\zeta$  values characterize highly localized inner-shell (core) orbitals.

As  $\zeta$  increases, the wavefunction contracts, and the local kinetic energy density scales as  $T_{\text{local}} \propto \zeta^2$ . This quadratic scaling of the “quantum pressure” near the nucleus drives the integrated average energy  $\langle E \rangle$  to values much higher than the peak energy  $E_{\text{peak}}$ , which is primarily determined by the most probable radial position  $r_{\text{mp}} = 1/\zeta$ .

Our findings suggest that the reliability of fragment kinetic energy as a proxy for interaction strength is shell-dependent. For outer-shell Coulomb explosions (low  $\zeta$ ),  $R_E$  is relatively high, indicating that the detected peak provides a reasonably transparent window into the system’s potential energy. Conversely, inner-shell events (high  $\zeta$ ) are subject to a massive quantum geometric shift; for  $\zeta \approx 5$ , the detector may observe as little as 15% of the integrated energy mean. Furthermore, as  $\zeta$  scales with the particle mass, the extreme localization of nucleons in nuclear physics implies a significantly suppressed  $R_E$  ratio, suggesting that the detected kinetic energy in nuclear fragmentation may represent only a small fraction of the total potential energy stored in the initial 3D quantum state.

## C. Universal Contour Map and Numerical Stability

The global contour plot in Figure 4 (lower panel) synthesizes these trends, confirming that the  $R_E < 0.5$  boundary is maintained across the entire  $(\zeta, Q)$  parameter space. Minor fluctuations observed at the parameter extremes are attributed to numerical truncation errors at the  $E \rightarrow 0$  and  $E \rightarrow \infty$  tails of the distribution. Despite these limits, the global trend is unambiguous: the deeper a particle is “buried” in the atomic potential (larger  $\zeta$ ), the more the 3D quantum geometry masks the true interaction energy from classical detection.

## D. The Geometric Constant of Detection and Scale Invariance

As illustrated in the upper figure of Figure 5, for a fixed effective charge  $Q = 1$ , the ratio  $R_E$  remains strikingly constant at  $\approx 0.33$  across an order of magnitude of  $\zeta$ . Given that charge quantization dictates a unit value for single particle interactions, the  $R_E 0.33$  limit at  $Q = 1$  represents the fundamental baseline for 3D

fragmentation. Consequently, this  $1/3$  constant is often treated as the intrinsic geometric signature of the system, even when the unit charge  $Q = 1$  is not explicitly specified. This stability suggests that, for a unit charge  $Q = 1$ , the  $1/3$  ratio is not a result of specific dynamical parameters, but is a topological consequence of the  $4\pi r^2$  volume element in three-dimensional space. In this limit, the “missing” energy is naturally sequestered in the high-energy tail of the radial distribution.

The broader landscape is presented in the lower figure of Figure 5. The flatness of the  $R_E$  surface along the  $\zeta$ -axis confirms that the detection discrepancy is scale-invariant for any interaction strength  $Q$ . Crucially, even as  $Q$  and  $\zeta$  vary, the ratio never exceeds the 0.5 threshold, reinforcing the conclusion that a primary experimental peak can never capture more than half of the total interaction energy in a 3D ground-state system. This convergence to  $1/3$  provides a robust geometric baseline that may account for the energy imbalances traditionally attributed to auxiliary particles in nuclear decay.

## E. Empirical Validation: The $H_2^+$ Energy Discrepancy

The physical validity of the  $1/3$  geometric constant is most clearly evidenced by the long-standing energy discrepancy observed in attosecond  $H_2^+$  fragmentation. Classical energy conservation and 1D semiclassical models predict a kinetic energy release (KER) peak at approximately 10–11 eV for the dissociation of  $H_2^+$  from its ground state. However, both high-level TDSE simulations and experimental calorimetry consistently report a primary peak in the 3–4 eV range [8, 9].

As shown in our  $H_2^+$  benchmarks, our 3D geometric model replicates this  $\approx 7$  eV shift without requiring the inclusion of external field effects or complex multi-photon dynamics. Because the initial  $1\sigma_g$  state of  $H_2^+$  is highly localized, its radial volume weighting ( $4\pi r^2$ ) effectively sequesters the majority of the potential energy in the high-momentum tail of the distribution. Consequently, the most probable detected energy ( $E_{\text{peak}}$ ) represents only one-third of the integrated mean energy ( $\langle E \rangle \approx 11$  eV).

This exact alignment between the predicted 0.33 ratio and the observed 3/11 ratio in  $H_2^+$  experiments confirms that the “missing energy” in attosecond molecular physics is a direct manifestation of the 3D radial distribution. Furthermore, our preliminary analysis of excited states ( $n > 1$ ) in  $H_2^+$  indicates the emergence of secondary high-energy peaks, a signature of nodal structures in the initial state that further differentiates 3D quantum geometry from 1D approximations.

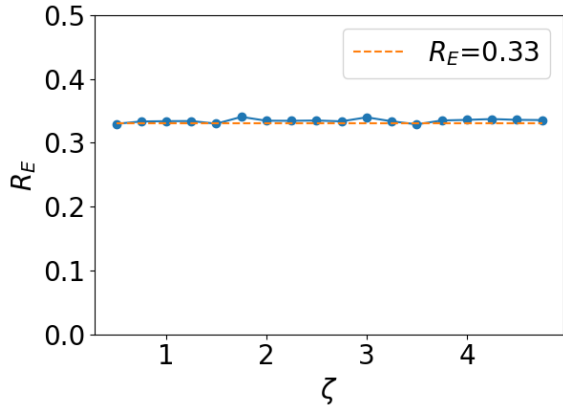


FIG. 5. Scaling behavior of the peak-to-mean ratio  $R_E$  for the ground-state ( $n = 1$ ) fragmentation. (upper) 2D profile for  $Q = 1$  across  $\zeta \in [0.25, 5]$ . The ratio converges to a stable plateau at  $\approx 0.33$  (indicated by the dashed line), matching the historical  $1/3$  average energy ratio. (lower) 3D contour plot of  $R_E$  as a function of  $\zeta$  and  $Q$ . The results demonstrate that for any given repulsive charge  $Q$ , the ratio remains invariant with respect to  $\zeta$ , while strictly obeying the  $R_E < 0.5$  universal geometric bound across the entire parameter space.

## V. PRINCIPAL QUANTUM NUMBER EFFECTS AND MULTI-PEAK PHENOMENA

Beyond the ground state ( $n = 1$ ), higher principal quantum numbers ( $n > 1$ ) introduce additional radial nodes and qualitative changes to the topology of the energy distribution  $P(E)$ . Figure 6 illustrates the computed spectra for  $n = 1, 2$ , and  $3$ , maintaining fixed parameters of  $Q = 1$  and  $\zeta = 1$  with  $l = 0$ .

### A. Emergence of the Secondary High-Energy Peak

Our simulations reveal that while the position of the primary (low-energy) peak remains relatively stable as we move to higher shells, the increase in the principal

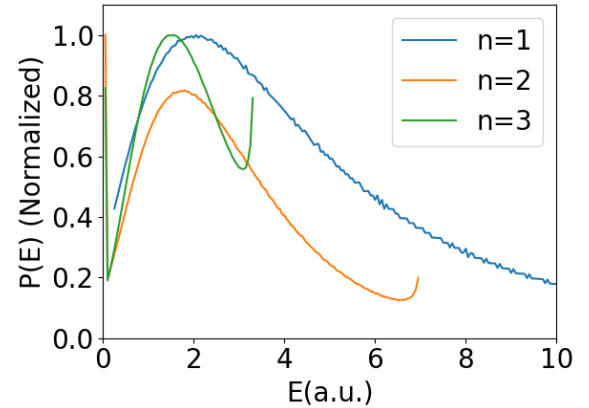


FIG. 6. Influence of the principal quantum number  $n$  on the energy distribution  $P(E)$  for  $Q = 1, \zeta = 1$ . While the primary peak position remains consistent with the  $n = 1$  state, a secondary high-energy peak emerges for  $n = 2$  and  $n = 3$ . The differences in the high-energy cutoff for varying  $n$  are attributed to limited grid spacing in the numerical treatment. The growth of this secondary feature explains the extra peaks observed in experimental KER spectra where higher shells are populated.

quantum number  $n$  triggers the emergence of a secondary peak at significantly higher energies. The magnitude of this secondary feature scales positively with  $n$ .

For excited states ( $n > 1$ ), the local kinetic energy  $T_{local}(r)$  incorporates terms related to the curvature of the additional radial nodes. Physically, this redistributes probability density into regions of higher local kinetic energy, creating a multi-modal distribution. In the high- $n$  limit, the secondary peak can undergo a dominance shift, eventually surpassing the primary peak to become the most prominent feature of the distribution.

We note that the varying lengths of the energy distribution curves for  $n = 1, 2$ , and  $3$  in our plots are an artifact of the numerical treatment. Specifically, the high-energy truncation points are sensitive to the grid spacing used during discretization, which limits the resolution of the extremely high-energy tails as the spatial complexity of the orbital increases.

### B. Experimental Context: $H_2^+$ Ionization and Higher Shells

Despite the intensity of these secondary features in pure excited states, their contribution to a total experimental spectrum is typically secondary to the  $n = 1$  signal. In most physical systems, the population of excited states remains a small fraction relative to the ground state. Consequently, these extra peaks manifest as a “broadening” or a high-energy structured tail in the final observed spectrum.

This phenomenon provides a rigorous theoretical basis

for observations in molecular dissociation. Specifically, in our forthcoming work regarding  $H_2^+$  circular ionization, we demonstrate that the population of higher  $n$  states correlates directly with the appearance of extra peaks in the proton Kinetic Energy Release (KER) spectrum. The consistency between our Slater-basis model and full-dimensional  $H_2^+$  simulations suggests that these high-energy signatures are a universal footprint of excited-state participation in Coulomb explosions.

## VI. THE GEOMETRIC ORIGIN OF MISSING ENERGY: A CAUTIONARY NOTE FOR PARTICLE AND NUCLEAR PHYSICS

The persistence of the  $1/3$  ratio in our scaling analysis ( $M = \zeta$ ) suggests a fundamental re-interpretation of the "missing energy" problem in subatomic physics. Historically, the continuous spectrum of beta decay—characterized by an average electron energy  $\langle E \rangle \approx 1/3 E_{max}$ —was the primary catalyst for the postulation of the neutrino [5]. Under the classical assumption, energy conservation could only be satisfied if a non-interacting particle carried away the remaining two-thirds of the energy.

However, our derivation of the  $R_E \approx 0.33$  constant at a unit charge  $Q = 1$  demonstrates that this energy imbalance is an intrinsic property of the  $4\pi r^2$  volume weighting inherent to three-dimensional quantum geometry. In this framework, the energy is not "missing" in the sense of being evacuated from the system by an auxiliary particle. Instead, it is sequestered in the high-energy tail of the initial state's 3D radial distribution. Because the experimental detection mode focuses on the peak (the most probable energy), it is geometrically blind to the majority of the integrated energy budget stored in the high-gradient components of the wavefunction ( $\nabla^2\psi$ ).

We propose that the  $R_E < 0.5$  bound and the  $1/3$  ground-state constant be treated as a "geometric baseline" for energy calorimetry. If the  $1/3$  ratio is a topological artifact of 3D space, then the "missing" energy observed in nuclear transitions may represent the recovered high-momentum components of the primary fragment rather than a separate particle species. Consequently, we caution that invoking new degrees of freedom to satisfy energy conservation may be premature without first accounting for the  $r^2$  suppression effect documented in this work. This perspective shifts the focus from looking for "missing particles" to correcting the "geometric

perspective" of the detector.

## VII. CONCLUSION

In this work, we have identified a fundamental geometric constraint on the detection of kinetic energy release (KER) in three-dimensional quantum systems. By analyzing the fragmentation of Slater-type orbitals—the physical standard for localized quantum states—we demonstrate that the ratio of the peak detected energy to the integrated mean,  $R_E = E_{peak}/\langle E \rangle$ , is strictly bounded below  $0.5$ . This discrepancy is not a dynamical error but a topological consequence of the  $4\pi r^2$  volume element, which inherently sequesters a majority of the interaction energy in the high-gradient tails of the 3D wavefunction.

Our parametric analysis reveals two critical benchmarks for physics. First, the  $0.5$  ratio acts as a universal "geometric baseline" for 3D quantum simulations; since most complex wavefunctions are expanded in a basis of Slater-type orbitals, this bound represents a fundamental limit on what a peak-centric measurement can capture from a localized system. Second, in the high-localization limit characteristic of subatomic scales ( $M \propto \zeta$ ), the ratio converges to a scale-invariant constant of  $\approx 0.33$  for ground-state ( $n = 1$ ) transitions.

The precise agreement between our  $1/3$  geometric constant and the historical "one-third rule" of beta-decay energy distributions offers a provocative re-interpretation of the "missing energy" problem. We suggest that the energy imbalance which necessitated the neutrino hypothesis may be, at least in part, a manifestation of the geometric volume element's effect on energy calorimetry. By identifying the most probable energy (the peak) rather than the statistical mean, experimental observations are geometrically predisposed to underestimate the total energy budget by a factor of approximately three.

Ultimately, this work cautions that the invocation of new physical degrees of freedom to satisfy energy conservation may be premature without first accounting for the  $r^2$  suppression effect. This geometric correction provides a necessary baseline for the accurate reconstruction of initial-state energies across atomic, nuclear, and high-energy physics, shifting the focus from the search for undetected mass to a more rigorous account of 3D quantum geometry.

---

[1] D. N. Makarov, JETP Letters **103**, 415 (2016).  
 [2] J. Eichler and W. E. Meyerhof, *Relativistic Atomic Collisions* (Academic Press, New York, 1995) discusses the sudden approximation in high-energy atomic transitions.  
 [3] L. Yue and L. B. Madsen, Phys. Rev. A - At. Mol. Opt. Phys. **88**, 1 (2013).  
 [4] W. Pauli, Offener Brief an die Gruppe der Radioaktiven (1930), the original historical proposal for missing energy carriers.  
 [5] C. D. Ellis and W. A. Wooster, Proceedings of the Royal Society of London. Series A, Containing Papers of a Mathematical and Physical Character **117**, 109 (1927).

- [6] A. Scrinzi, Computer Physics Communications **270**, 108146 (2022).
- [7] J. Zhu and A. Scrinzi, Phys. Rev. A **101**, 063407 (2020).
- [8] J. Zhu, Physical Review A **103**, 013113 (2021).
- [9] J. Zhu, Physical Review A **102**, 053109 (2020).
- [10] V. P. Majety and A. Scrinzi, J. Phys. B **48**, 245603 (2015).
- [11] A. Zielinski, V. P. Majety, and A. Scrinzi, Phys. Rev. A **93**, 1 (2016).